# Porous Triangular Structure's Drag Coefficient as a Submerged Obstruction in Open Channels

**Ira Widyastuti**
Department of Civil Engineering, Faculty of Engineering, Cenderawasih University, Papua 99332, Indonesia
iwidyastuti09@gmail.com (corresponding author)

**Riswandy Loly Paseru**
Department of Civil Engineering, Faculty of Engineering, Cenderawasih University, Papua 99332, Indonesia
riswandylolypaseru@gmail.com

*Received: 24 March 2025 | Revised: 5 May 2025 and 11 May 2025 | Accepted: 15 May 2025*

 *DOI: https://doi.org/10.48084/etasr.11115*

## ABSTRACT

**This research aims to dampen energy without causing significant erosion around the obstacle models. Experiments were conducted on a square channel using three models of triangular plates (MP1, MP2, MP3) with a 30° slope and different levels of porosity (0, 10, and 15%). The flow channels around the energy obstacles were measured to assess different areas of the obstacle structure, depending on the channel characteristics and Reynolds number, using the drag coefficient ($C_D$). Frictional forces were attributed to shear stress on the surface of solid objects moving through a viscous fluid. The results showed that the effect of energy-absorbing porous materials on reducing flow velocity before passing through the obstacles varied across models: a 31.42% decrease in MP1, a 9.27% increase in MP2, and a 32.92% increase in MP3. The average flow velocity after passing through MP1, MP2, and MP3 increased significantly by 37.80%, 25.00%, and 43.85%, respectively. The drag coefficient ($C_D$) of porous obstacles was calculated by comparing the measured drag coefficients across models, resulting in a similar average across models, amounting to 4.82 (MP1), 4.03 (MP2), and 3.76 (MP3). The Reynolds number was $3.7x10^5$ – $7.4x10^5$, indicating the presence of laminar, transitional, or turbulent boundary layers.**

***Keywords- porous triangle structure; drag coefficient; flow reduction***

## I. INTRODUCTION

The estimation of drag force action on the surface of an object has drawn attention in Hydraulic Engineering and Eco-hydraulics fields. Despite extensive research, there is not an adequate amount of strategies to decrease drag force in several flow settings [1]. Turbulence in fluid dynamics is a common phenomenon characterized by a spontaneous transition from smooth laminar flow to rapid, irregular dynamics [2]. High-frequency drag dominates drag force variance for small protrusions, but low-frequency fluctuations become more significant as protrusion size increases [3]. Drag force is associated with frictional force and the consequences of increasing or decreasing the velocity of wind, gas, or water flows. Some studies dealing with drag force on object surfaces have modified the wall structures into an object that can or cannot be wetted, or have created a Cassie-Baxter model (hydrophobic, riblets) by producing different textures to catch minuscule drops of vapor [4]. It is the fundamental force influenced by an object in the face of movements. The drag force resulting from friction is caused by shear stress on the surface of a solid object moving through a viscous fluid [5]. The former can be reduced significantly by 27% in circular disc geometries with low depth ratios as the Reynolds number increases [6].

The lift and pressure coefficients are calculated to predict pressure and velocity distribution, providing insights into the correlation between Reynolds number and flow alterations. In [7], it was explained that polymers can reduce resistance beyond the asymptotic limit, eliminate turbulence, and allow for laminar flow, demonstrating that the former is dynamically disconnected from regular turbulence. Prior research has shed light on the remarkable ability of polymers to diminish resistance forces in fluid dynamics to an extent exceeding the typically accepted asymptotic boundary. Also, polymer addition has been shown to effectively suppress or even completely diminish turbulent flow patterns. This suggests a dynamic separation between the flow behavior near the asymptotic boundary, which exhibits a distinct suppression of turbulence, and the fully developed turbulence seen at higher Reynolds numbers, implying independent governing mechanisms. The other way to illustrate different flow regions and flow dependency on Reynolds number is the drag concept, where a friction force is generated by sheer stress on the

surface of a solid object perforating a viscous fluid [8]. As the object shape affects the drag force, introducing a ridge parallel to a cross-flow wavelength that stretches between five and eight viscous units, which can reduce surface obstacles. Water plays a key role by infusing a liquid ratio of O(1), resulting in a 14% reduction in drag on the object's surface [9]. The impact of obstacle height on gravity currents traversing embankment barriers of varying heights was investigated in both subcritical and supercritical flow regimes [10]. According to [1], the turbulent friction on the solid/liquid interface is responsible for an enormous loss of energy that channels the liquid through the hydraulic network, contributing to around 10% of the global electricity consumption. While aquatic vegetation provides ecological benefits, it brings several drawbacks to the environment, such as making the flow resistance higher, water levels rise, and risk of flooding heightens from a hydraulic perspective [11].

Authors in [12] used lubricant fluid on a textured surface to obtain a more slippery surface, reducing obstacles in laminar flow by 16%. In addition, natural structures, like mangroves and bamboo, protect coastal areas from floods and erosion by forming short-range anisotropic structures and separating enormous flow to maximize the drag coefficient and reduce dissipated energy by 20% [13]. If the fluid flows to the wood's pores, the wood transports allow more efficient wood processing and a more sustainable usage [14]. Observations of local skin-friction reduction reveal noticeable peaks occurring specifically at the downstream limit of the area where actuation is applied. This peak formation suggests that the process of diminishing turbulence extends over a longer distance when the flow possesses a higher Mach number. Accordingly, a more gradual shift from turbulent to laminar or less turbulent conditions occurs. In general, the Reynolds stresses, which are a measure of turbulent fluctuations, are diminished within the flow field. However, not all stress components are reduced the same because a more pronounced effect is observed in the streamwise direction for the specific case of M = 0.7 [15]. Understanding how drag force works against porous obstacles enables the calculation of the obstacle force.

Authors in [16] reported that a wide channel will create secondary channels due to increased obstacles in the flow, resulting in different flow distributions in a narrower channel [16]. The turbidity current entered the porous sheet and porous obstacle differently; longitudinally in the former and perpendicularly in the latter. The results indicated a key distinction in the behavior of turbidity currents when interacting with different types of porous media. More specifically, the implementation of porous obstacles led to the formation of a distinctive rotational flow pattern. This flow, which occurs when two perpendicular sides give way to turbidity currents, encountered the three-dimensional structure of the obstacle. This flow pattern was crucial in promoting energy dissipation within the turbidity current. As opposed to the application of layers with porosity, the energy of the current was more effectively dissipated when using obstacles with porosity [17]. The study of frictional velocity shows a clear pattern linked to the pore opening model, indicating a strong connection between how the flow behaves and the amount of pore openings in the model. As the number of pore openings increases in the simulated environment, the speed of the flow slows down before it hits the obstacle. In other words, data suggest that the flow, as it exists upstream from the impediment, weakens or decreases in magnitude as the density of pore openings rises [18].

Dimensional analysis, a method to address physical quantity dimensions, is suitable for problems in fluid mechanics and hydraulics. Dimensional analysis enables the search and determination of the desired correlation between variables. It is deployed in determining the correlation between variables in the hydraulic model test, as long as accurate variable data are used [19].

This study performs a quantitative analysis of the flow through pores with varying slopes, illustrating the magnitude of resistance on the surface of porous structures.

## II. THE PROPOSED APPROACH

### *A. Velocity Distribution and Flow Patterns in a Porous Triangular Structure*

The flow velocity, a three-pronged way, varies significantly from one point in an open channel to another according to Cartesian coordinates. Since the first two directions (vertical and lateral) are considered insignificant, only the regular direction is counted [20]. Analyzing the flow characteristics in the energy dissipater structure can be quite challenging. Therefore, this study deploys an empirical approach to identify the flow velocity distribution in both the inner and outer regions [21]. In the former, the velocity is controlled by the friction velocity, expressing the actual velocity distribution:

$$\frac{u(z)}{U_m} = \left(\frac{z}{D_m}\right)^{\frac{1}{\alpha_v}} \quad (1)$$

In the latter, friction velocity on the water surface boundary controls the velocity. The velocity distribution is defined using a semi-Gaussian relationship [21]:

$$\frac{u(z)}{U_m} = exp\left[-\beta_v \left(\frac{z - D_m}{D - D_m}\right)^{\gamma_v}\right] \quad (2)$$

where $u(z)$ is the average velocity at a distance z from the base and is measured in cm/s, $U_m$ is the maximum flow rate in $cm^3/s$, and $D_m$ is the upper limit of the maximum velocity ($z = D_m$) [22]:

$$\alpha = \frac{\Sigma v^3 \Delta A}{v^3 A}$$

$$\beta = \frac{\Sigma v^2 \Delta A}{v^2 A}$$

where $a_v$ is the value of the vertical direction energy coefficient, $\beta_v$ is the coefficient of the vertical direction energy momentum, $v$ is the velocity in cm/s, and $A$ is the wet cross-sectional area in $cm^2$.

In (2), $\beta_v$ is the energy momentum coefficient, $\gamma_v$ is the result of the exponential function with a logarithmic base variable, and $D$ is the average flow height limit, as shown in Figure 1.

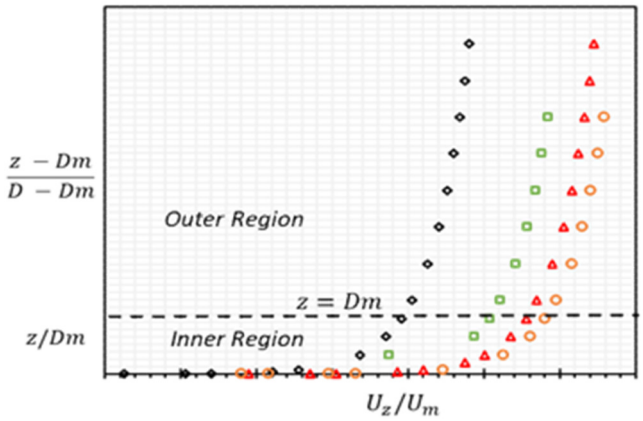


Fig. 1. Illustration of the non-dimensional flow velocity profile.

### B. Hydrostatic Force on a Barrier

In general, a force has three attributes: magnitude, point of application, and direction of action. The magnitude of the hydrostatic force F acts on an arbitrary surface area and forms an angle $\theta$ with the water surface, as shown in Figure 2. Consider the force acting on the area of the strip d$A$, which is equal to the pressure on the strip p multiplied by the area of the strip d$A$ or $dF = p\,.\,dA = \gamma\,.h\,.\,dA$. By summing all the forces acting on that arbitrary surface area, considering that $h = y.\sin\theta$ because $h_s = y_s\,sin\,\theta$, the equation is:

$$F = \rho g\, h_s\, A \quad (3)$$

where $F$ is the hydrostatic force (N), $\rho$ is the density (kg/m$^3$), $g$ is the acceleration due to gravity (m/s²), $h_s$ is the depth of the field center relative to the water surface (m), and $A$ is the area of the object surface (m$^2$).

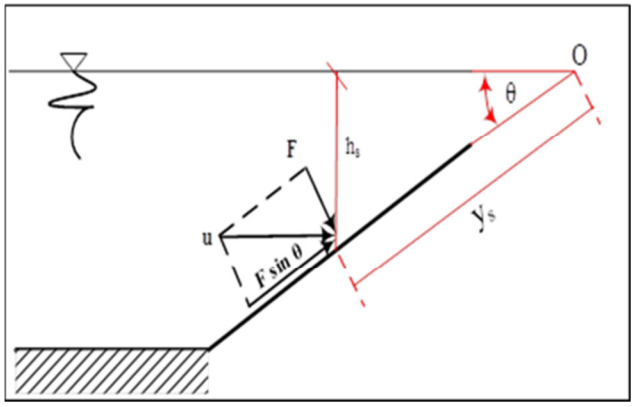


Fig. 2. Hydrostatic force on an arbitrary angled plane $\theta$.

### C. Drag Force ($C_D$) on a Porous Structure

Drag force is caused by friction due to shear stress acting on the exterior of a solid object perforating a viscous fluid. The frictional drag is calculated as:

$$\frac{F}{A} = C_f \frac{\rho v^2}{2} \quad (4)$$

where $F$ is the frictional force, $A$ is the contact area between the object and the fluid, $C_f$ is the skin friction coefficient, $\rho$ is the fluid density, $v$ is the free stream fluid velocity. Meanwhile, the total drag on an object can be caused by pressure or by the influence of friction. In such situations, another coefficient $C_D$ is defined as :

$$\frac{F}{A_p} = C_D \frac{\rho v^2}{2} \quad (5)$$

where $C_D$ is the drag coefficient and $A_P$ is the projected surface area. The quantity of $\frac{\rho v^2}{2}$ is the value of the dynamic pressure.

Another way to describe different flow regions and the dependence of these flows on the Reynolds number is through the concept of drag in which frictional force is caused by shear stress imposed by the exterior face of a non-liquid matter when perforating viscous liquid [8].

### D. Dimensional Analysis

#### 1) Basic Principles

This research aims to assist in solving problems in the field of engineering, as well as in other study areas that use a dimensional analysis approach, which involves the following steps: First, it identifies the important independent (non-dependent) variables, and then determines the number of non-dimensional independent variables created from the variables. Finally, it reduces the number of system variables to obtain the correct set of non-dimensional independent variables [23].

#### 2) Formation of Dimensionless Variables

- The use of dimensionless variables helps minimize the number of variables subjected to investigation through experiments, field analysis, or numerical measurements.
- A dimensionless graph provides more information than a graph with dimensions because the former allows for a wider range of variables.
- The points in a dimensionless graph can often be obtained from a scale model.
- The dimensionless product is a feasible archetype for model scale planning and result interpretation.
- The results and analysis of the dimensionless model developed in this study are presented in a concise and systematic manner. Various physical quantities can be expressed in terms of fundamental dimensions—mass, length, and time. From these fundamental dimensions all other quantities are derived.

#### 3) Buckingham π Method

Methods for determining dimensionless numbers include the Buckingham π method, the indicial matrix method [23], Rayleigh's method, the stepwise procedure, and the Langhaar method. The Buckingham $\pi$ method states that if a phenomenon involves $n$ dimensional variables that can be described using $m$ fundamental dimensions, then the relationship among these variables can be expressed using ($n$ – $m$) independent, dimensionless variables ($\pi$ terms). According to the Buckingham method, applied in hydraulic models, if a function consists of $n$ parameters, these parameters can be grouped into a set of independent dimensionless ratios, known

as parameter $\pi$, and can be expressed as function of $G$ ($\pi_1$, $\pi_2$,……,$\pi_{(n-m)}$)= 0, where $m$ is the repeated parameter, which usually (but not always) equals with $r$, and $r$ is the minimum number of free dimensions to specify the dimensions of all parameters.

## III. EXPERIMENT SET-UP

This study established that a horizontal rectangular canal has a friction resistance against supercritical flow distribution that will dampen the flow energy, thus decelerating velocity and increasing the height of the flow direction. Therefore, an energy dissipation structure placed in the rectangular channel aims to inhibit the flow velocity at the channel bed.

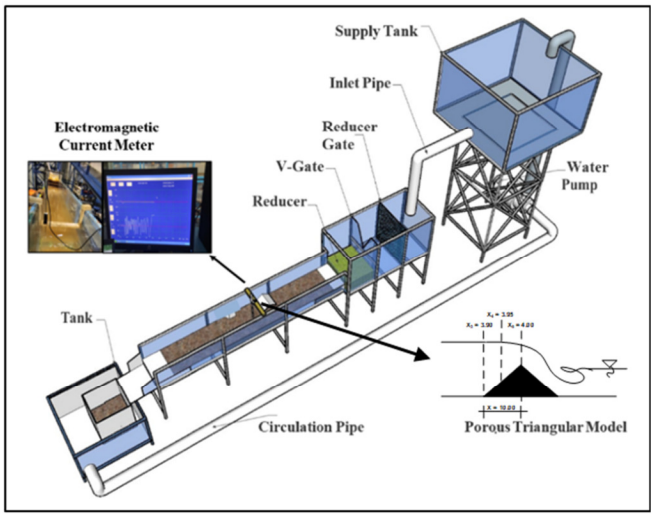


Fig. 3. Experimental scheme in an open channel.

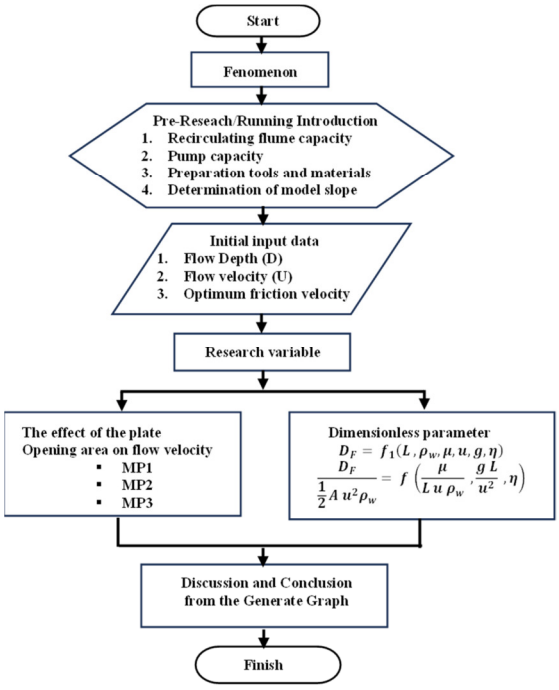


Fig. 4. Flowchart of experimental procedure.

The average maximum velocity was utilized to identify the plate height, 0.6$D$ from the average water surface height, and approximately 10.90 cm from the channel bottom. This resulted in a plate height of 6.00 cm with pore variations in MP1, MP2, and MP3 by 0%, 5%, and 10%, respectively, relative to the plate area. The plates were positioned 4.00 m ($x$) from the inlet, and the flow velocity was measured in 24 readings at eight distances—$x_1$ through $x_8$—corresponding to 3.50, 3.90, 3.95, 4.00, 4.25, 4.50, 5.00, and 5.50 m, respectively, along the bed slope. The open channel at the upstream section has an approximate upstream boundary condition depth of flow ($D$) of ≈11.00 cm and a downstream boundary condition of ≈ 8.00 cm. The flow velocity was measured with ADV [24].

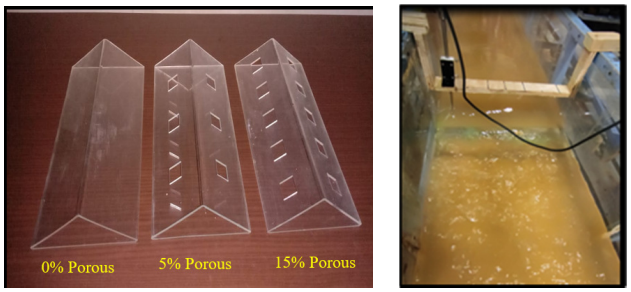


(a) (b)

Fig. 5. (a) Triangular obstacle model with pore variation, (b) flow velocity measurement with triangular obstacle.

## IV. RESULTS AND DISCUSSION

### A. Analysis of Drag Coefficient ($C_D$)

In the implementation of flow velocity measurements due to the presence of energy dissipation structures, each influential variable was selected based on three fundamental dimensions: mass (M), length (L), and time (T), with eight variables ($n$) and three fundamental units ($r$), resulting in five dimensionless constants ($n - r$). Table I presents the variables contributing to drag force ($C_D$).

The recurring variables, the ones with $M$, $L$, and $T$, are $\rho_w$ ($ML3$), $u$ ($LT$-1), and $L$ ($L$). The $\pi$ variable equation is the product of multiplying three repeated variables, while one variable remains, and so on until all variables are accounted for. Based on the variable grouping in Table I, five forms of dependent variables can be derived. The first $\pi$ term is formed from dependent variable 1:

$$\pi_1 = L^a u^b \rho_w^c F(L)^{a1} (LT^{-1})^{b1} (MT^{-3})^{c1} (MLT^{-2})^{c1}$$

$$L^{a1} L^{b1} T^{-1b1} M^{c1}\, L^{-3c1} MLT^{-2}$$

And then find $a$, $b$, and $c$ by:

$$M \Rightarrow 0 = c_1 + 1 \Rightarrow c1 = -1$$

$$T \Rightarrow 0 = -b_1 + (-2) \Rightarrow b_1 = -2$$

$$L \Rightarrow 0 = a_1 + b_1 - 3c_1 + 1 = a_1 - 2 + 3 + 1 \Rightarrow a_1 = -2$$

Then, $\pi_1 = \frac{F}{L^2\, u^2 \rho_w}$, as depicted in Table II, presents five dependent variables formed from the equation. The simplified version of this equation is:

$$\pi_1 = \frac{\pi_1}{\pi_4} = \frac{F}{L^2\, u^2 \rho_w} \times \frac{L^2}{A} = \frac{F}{A\, u^2 \rho_w}$$

The function for the variables is:

$$f(\pi_2, \pi_3, \pi_5, \pi_6) = \left(\frac{\mu}{L\, u\, \rho_w}, \frac{g\, L}{u^2}, \eta, \frac{F}{A\, u^2 \rho_w}\right) \quad (6)$$

The correlation that occurs is given by:

$$\frac{F}{A\, u^2 \rho_w}\ VS\ \frac{L\, u\, \rho_w}{\mu}; \frac{F}{A\, u^2 \rho_w}\ VS\ \frac{g\, L}{u^2} \quad (7)$$

TABLE I. VARIABLES OF DRAG FORCES ($C_D$)

| Dimension | Forces (*DF*) | Style (*L*) | Density ($\rho$) | Viscosity ($\mu$) | Velocity (*u*) | Gravity (*g*) | Area of plate (*A*) | Geometric shape ($\eta$) |
|---|---|---|---|---|---|---|---|---|
| M | 1 | 0 | 1 | 1 | 0 | 0 | 0 | 0 |
| L | 1 | 1 | -3 | -1 | 1 | 1 | 2 | 0 |
| T | -2 | 0 | 0 | -1 | -1 | -2 | 0 | 0 |

TABLE II. DEPENDENT VARIABLES FORMED

| Variable-1 | Variable-2 | Variable-3 | Variable-4 | Variable-5 |
|---|---|---|---|---|
| $\pi_1 = \frac{F}{L^2\, u^2 \rho_w}$ | $\pi_2 = \frac{\mu}{L\, u \rho_w}$ | $\pi_3 = \frac{gL}{u^2}$ | $\pi_4 = \frac{A}{L^2}$ | $\pi_5 = \eta$ |

TABLE III. VELOCITY DISTRIBUTION BASED ON REGIONAL DIVISION

| Distribution of flow zone | Measure Data MP1 | | | Distribution of Velocity Zone | | | | | | | |
|---|---|---|---|---|---|---|---|---|---|---|---|
| | *X* = 3.75 | | | $Z/D_m$ | $\gamma_u$ | β | α | Inner region $\frac{u_z}{U_m} = \left(\frac{z}{H_m}\right)^{\frac{1}{\alpha}}$ | Outer region $\frac{u_z}{U_m} = exp\left(-\beta v \left(\frac{z-H_m}{H-H_m}\right)^{\gamma v}\right)$ | $U_Z/U_m$ | $U_Z$ |
| | *z* | *D* | *U* | | | | | | | | |
| $Z / D_m$ | 0.50 | 11.20 | 19.54 | 0.25 | | | 6.08 | 0.80 | | 0.80 | 23.34 |
| | 1.00 | 11.20 | 21.92 | 0.50 | | | 8.18 | 0.92 | | 0.92 | 26.93 |
| | 1.50 | 11.20 | 27.38 | 0.75 | | | 15.16 | 0.98 | | 0.98 | 28.76 |
| Z | 2.00 | 11.20 | 29.31 | 1.00 \| 0.00 | | | 17.64 | 1.00 | 1.00 | 1.00 | 29.31 |
| $\frac{Z - D_m}{D - D_m}$ | 3.00 | 11.20 | 22.95 | 0.12 | 1.50 | 0.32 | | | 0.99 | 0.99 | 28.90 |
| | 4.00 | 11.20 | 19.77 | 0.28 | | 0.21 | | | 0.97 | 0.97 | 28.40 |
| | 5.00 | 11.20 | 27.68 | 0.48 | | 0.36 | | | 0.89 | 0.89 | 25.95 |
| | 6.00 | 11.20 | 20.55 | 0.77 | | 0.16 | | | 0.89 | 0.89 | 26.18 |
| | 7.00 | 11.20 | 29.04 | 1.19 | | 0.27 | | | 0.70 | 0.70 | 20.64 |
| | 8.00 | 11.20 | 23.63 | 1.88 | | 0.13 | | | 0.71 | 0.71 | 20.66 |
| | 9.00 | 11.20 | 22.37 | 3.18 | | 0.08 | | | 0.62 | 0.62 | 18.21 |
| *Average U* | | | 24.00 | | | | | | | | 25.21 |

### *B. Flow Velocity Distribution in the Channel*

The velocity ratio and velocity distribution ($U_Z$) respective to each region are measured in the middle span. In Table III, the measured data were for MP1 with *x*= 3.75 m and 4.20 m. Table III illustrates the distribution of each porous structure. Figure 6 (*a*, *b*, and *c*) shows the flow velocity patterns and distributions of the Clautser's Method before and after the obstruction. The obstacle models in this study were placed below the normal water surface, causing the water to rise upstream towards the obstacle.

A gently curved line ($\alpha$) in the inner region illustrates a decrease in flow velocity and tends to remain constant up to the height of the pore-free barrier, as seen in the velocity distribution pattern and graph in Figure 6(a). However, the curved line ($\alpha$) will enlarge, and the flow velocity will increase with the pore opening, as portrayed in Figures 6(b-c). When the flow is about to pass through the obstruction, a hydraulic jump ensues, and the flow velocity above the obstruction increases, as demonstrated in Figure 6(a).

However, the flow velocity above the triangular plate decreases when passing through the pores (Figure 6(b)), and the velocity will slightly increase if the pore opening is enlarged (Figure 6(c)).

A few moments after the flow passes the obstacle, turbulent flow occurs from the channel bed to the water surface due to the hydraulic jump around the obstacles, increasing the flow velocity, while the velocity pattern and distribution (*x*) reach 4.20, as displayed in Figure 6(a). The opposite results are observed when using porous plates because the pores will slightly retain the flow perforating the obstacle, thus reducing the flow velocity below the pores, as exhibited in Figure 6(b). In contrast, when the pore percentage increases, as the flow velocity moves through pores or obstacles it accelerates, as can be seen in Figure 6(c). The turbulent flow occurring around the obstacle will generate significant energy. Therefore, when the flow diverts the obstacles and reaches the inner region, it will speed down until it reaches the outer region. This occurs because the energy diminishes until the distance *x* is 5.0 m, as shown in Figures 6(a-c). The further away the flow from the obstacles is, the higher the energy will pick up, rendering/generating normal flows. The measurement of the obstacle area was conducted upstream of the porous triangular plate for each model—MP1, MP2, and MP3—and the results are presented in Table IV.

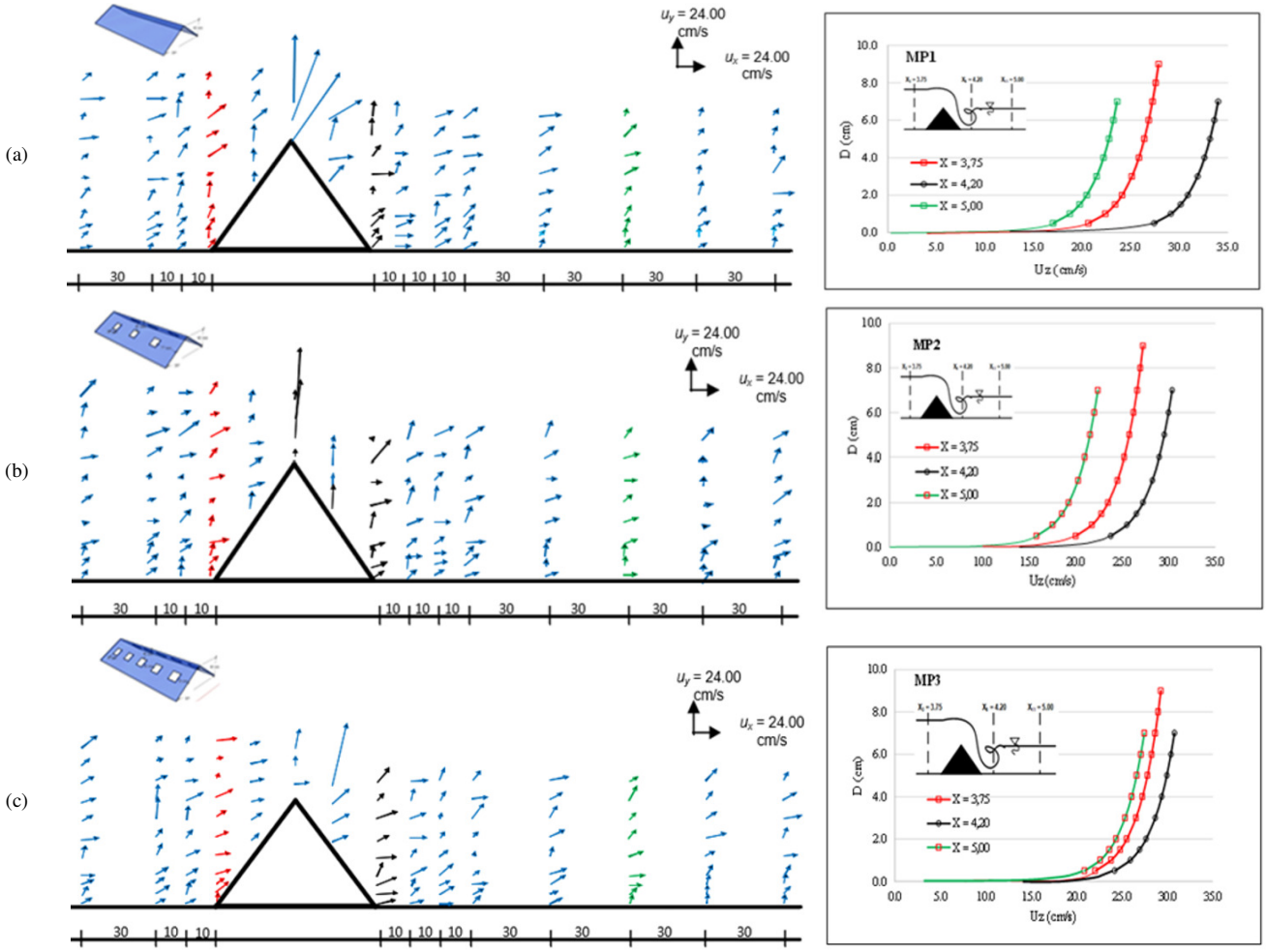


Fig. 6. Pattern and distribution of flow velocity ($u$) in porous energy absorbing structure.

TABLE IV. RESULTS OF FLOW VELOCITY (U) MEASUREMENTS ON THE UPSTREAM OF THE POROUS ENERGY DISSIPATING STRUCTURE

| **Distance (m)** | **MP$_1$** | **MP$_2$** | **MP$_3$** |
|---|---|---|---|
| x | 3.95 | 3.95 | 3.95 |
| z | | | |
| 4.00 | 19.616 | 32.340 | 34.109 |
| 5.00 | 23.920 | 34.073 | 35.842 |
| 6.00 | 32.589 | 35.087 | 36.855 |
| 7.00 | 31.814 | 35.806 | 37.575 |
| 8.00 | 24.896 | 36.364 | 38.132 |
| 9.00 | 27.073 | 36.820 | 38.588 |

Next, the measurement data were analyzed, and the results of the drag force ($C_D$) calculations with the Reynolds number ($Re$), as well as their relationship are presented in Table V and Figure 7. The drag coefficient that occurs will depend on the Reynolds number and the geometry of the object, specifically the contact area between the solid and the fluid. An increase in the contact area (A) will decrease the Reynolds number. In addition, from the relationship between $C_D$ and Re, a simple exponential analysis is undertaken, resulting in:

$$\frac{F}{\frac{1}{2}A\,u^2\,\rho_w} = 117.76\,e^{-6.E-0.5\,.\,Re} \quad (8)$$

TABLE V. CALCULATION OF REYNOLDS NUMBER ($Re$) AND DRAG FORCE ($C_D$)

| **MP$_1$** | | **MP$_2$** | | **MP$_3$** | |
|---|---|---|---|---|---|
| $\frac{L\,u\,\rho_w}{\mu}$ | $\frac{F}{\frac{1}{2}A\,u^2\rho_w}$ | $\frac{L\,u\,\rho_w}{\mu}$ | $\frac{F}{\frac{1}{2}A\,u^2\rho_w}$ | $\frac{L\,u\,\rho_w}{u}$ | $\frac{F}{\frac{1}{2}A\,u^2\rho_w}$ |
| 37482.81 | 12.19 | 46870.16 | 7.58 | 49433.16 | 6.62 |
| 38291.30 | 10.06 | 49381.56 | 5.85 | 51944.56 | 5.11 |
| 54291.55 | 4.19 | 50089.44 | 4.74 | 53413.64 | 4.00 |
| 72142.62 | 1.92 | 51624.40 | 3.57 | 54455.96 | 3.04 |
| 73611.69 | 1.40 | 59412.41 | 2.02 | 55264.45 | 2.18 |
| 74654.02 | 0.93 | 67165.69 | 1.05 | 55925.04 | 1.36 |

In (8), a calculation test of the drag coefficient ($C_D$) was conducted by comparing its measured values, which had similar average results, namely MP$_1$ = 4.82, MP$_2$ = 4.03, and MP$_3$ = 3.76, as shown in Table VI.

Different pore openings affect the flow passing through the obstacle. The resistance of a triangular plate with a slope of 30$^o$ shows that the $C_D$ value of a non-porous plate is 4.82, while in

plates with 5% and 10% pores, it is 4.03 and 3.76, respectively. That is, plates with 5% porosity are 63% better than those with 10% porosity in inhibiting water flow.

Figure 8 presents various drag coefficients against the Reynolds number for the sphere, infinite plate, circular disk, square plate, and porous triangular plate. The drag coefficient ($C_D$) value produced by the porous triangular plate is somewhat similar to the results of other plate studies. If the flow velocity measurement data are taken around the plate, the hydrostatic force ($F$) can be calculated using (8). The results of these calculations are exhibited in Table VII.

TABLE VI. COMPARISON OF $C_D$ VALUES

| | **MP$_1$** | | **MP$_2$** | | **MP$_3$** | |
|---|---|---|---|---|---|---|
| | y-meas. | y-cal. | y-meas. | y-cal. | y-meas | y-cal. |
| | 12.193 | 10.513 | 7.581 | 5.740 | 6.621 | 4.866 |
| | 10.061 | 9.979 | 5.854 | 4.883 | 5.114 | 4.139 |
| | 4.197 | 3.558 | 4.742 | 4.665 | 4.003 | 3.765 |
| | 1.920 | 1.126 | 3.571 | 4.225 | 3.049 | 3.520 |
| | 1.405 | 1.024 | 2.022 | 2.558 | 2.181 | 3.342 |
| | 0.939 | 0.958 | 1.055 | 1.552 | 1.369 | 3.202 |
| **Mean** | 5.119 | 4.526 | 4.137 | 3.937 | 3.723 | 3.806 |
| **Mean of $C_D$** | 4.823 | | 4.037 | | 3.764 | |

"meas" stands for measured, "cal" stands for calculated

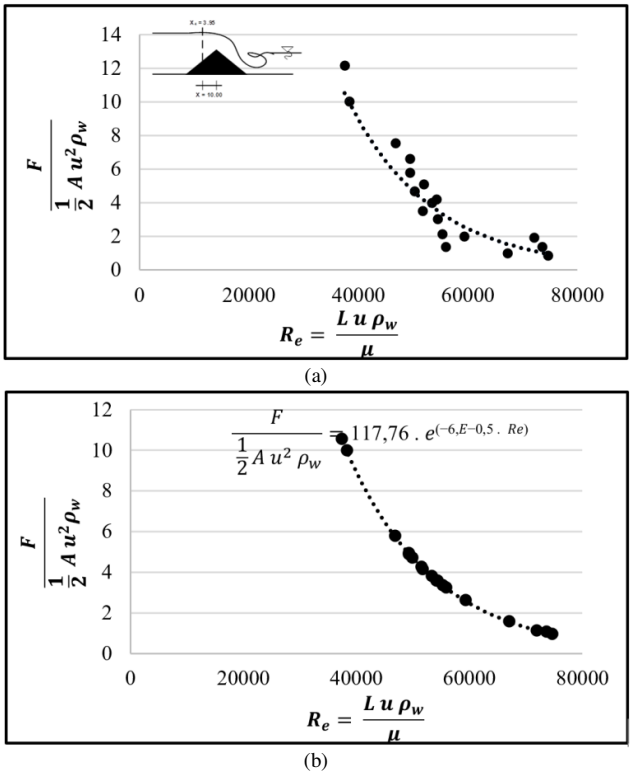


(a)

(b)

Fig. 7. (a) The relationship between drag force ($C_D$) and Reynolds number ($Re$), and (b) the relationship between $C_D$ and $Re$ after normalization.

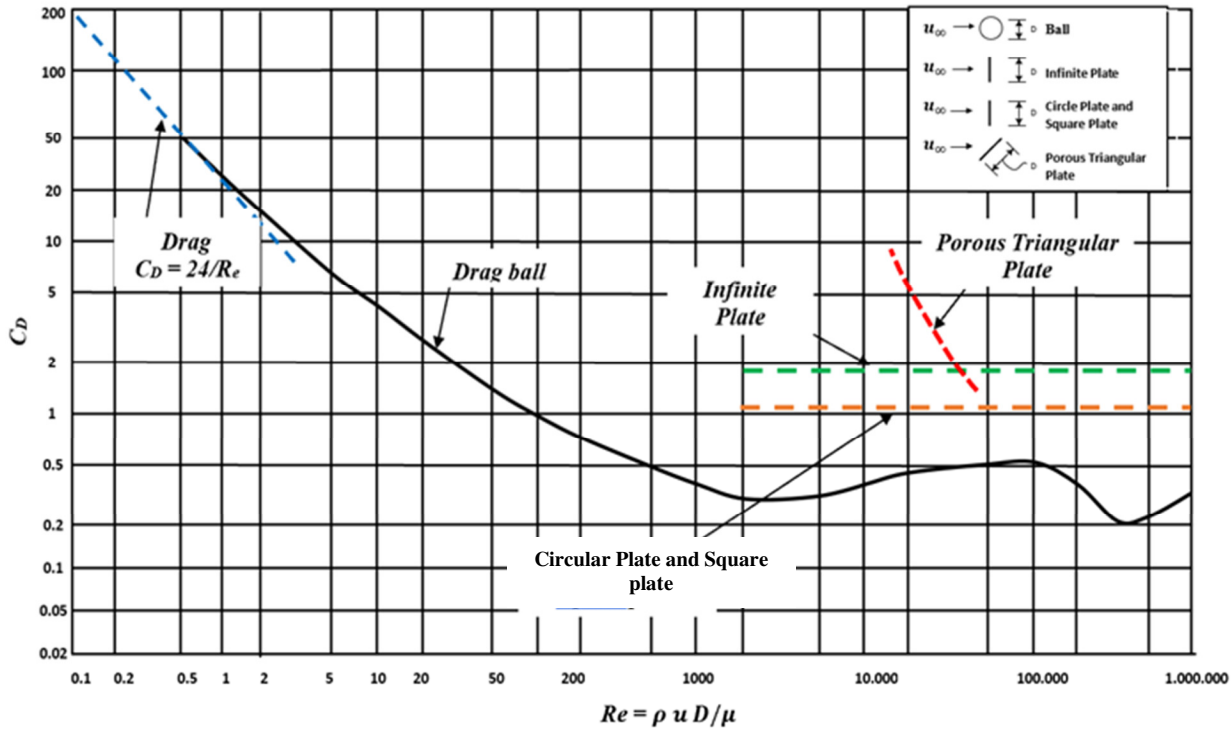


Fig. 8. Verification of drag coefficient ($C_D$) versus Reynolds number for various types of objects [8].

TABLE VII. COMPARISON OF CALCULATED FORCE-(*F*) AND MEASURED-FORCE (*F*)

| Model | Velocity measurement tata (u) | Average U | A | $\rho_w$ | $C_D$ | F-measured | F-calculated |
|---|---|---|---|---|---|---|---|
| | x = 3.95 | | | | | | |
| $MP_1$ | 25.86 | 40.30 | 480 | 1.00 | 4.82 | 1.88E+06 | 1.28E+06 |
| | 26.42 | | | | | | |
| | 37.46 | | | | | | |
| | 49.77 | | | | | | |
| | 50.79 | | | | | | |
| | 51.51 | | | | | | |
| $MP_2$ | 32.34 | 37.32 | 456 | 1.00 | 4.03 | 1.28E+06 | 1.16E+06 |
| | 34.07 | | | | | | |
| | 34.56 | | | | | | |
| | 35.62 | | | | | | |
| | 40.99 | | | | | | |
| | 46.34 | | | | | | |
| $MP_3$ | 34.10 | 36.85 | 432 | 1.00 | 3.76 | 1.10E+06 | 1.05E+06 |
| | 35.84 | | | | | | |
| | 36.85 | | | | | | |
| | 37.57 | | | | | | |
| | 38.13 | | | | | | |
| | 38.58 | | | | | | |

## V. CONCLUSION

This study examined how drag force is reduced in areas with obstacles. Drag forces were compared based on flow velocity in a channel featuring triangular structures as obstacles, which measured 6 cm in height, had a 30° slope, and a flow velocity of 24 cm/s. The structure plates had varying porosities: 0%, 5%, and 10% (designated as MP1, MP2, and MP3), relative to the plate's area. The findings revealed that the flow transitioned between laminar and turbulent states when the obstacles were placed at the bottom of the open channel below the surface.

The Reynolds number indicated that the velocity before the obstacles (upstream) declined by 31% in the non-porous structure (MP1), but it increased in the structures with 9% (MP2) and 32% (MP3) porosity. After flow velocity passed through (downstream) the obstacle, it increased by 37% (MP1), 25% in MP2, and 43% in MP3. Thus, it can be said that, if the pore opening is 10% of the plate area, the drag effect will diminish gradually. The most significant hydraulic jump occurred with MP1, while water flowing through the pores of MP2 and MP3 dampened the hydraulic jump from the top of the structures. This finding suggests that pore openings can help mitigate turbulent flow downstream, as evidenced in Figure 6.

Initially, the resistance value ($C_D$) of the disc or rectangular plate was between 1 and 2 at the channel bottom, slightly increasing when positioned upright and reaching between 3 and 4 on the porous triangular plates, as shown in Figure 8. Therefore, placing porous obstacles on the channel bed is the most effective method of reducing downstream flow velocity compared to non-porous triangular obstacles.

It shows potential risk management of flow exposed to high-velocity flow. Erosion around non-porous plates can create larger vortices, raising the risk of structural failure. To mitigate this risk, this study proposes tilting the plates and reducing porosity to less than 5%. Future studies should examine drag forces in unsteady flows, like tsunami waves and dam breaks that impact structures, and compare these findings with those of the present work to find out if the current relationships for immediate conditions are still valid. This innovative approach not only enhances energy efficiency, but also promotes sustainable practices in various engineering applications. By strategically arranging these barriers, fluid dynamics can be optimized and energy loss in systems where flow management is critical can be reduced. Additionally, it would be beneficial to characterize drag forces through pore openings and examine the effects of significant erosion on the channel bed.

## REFERENCES

[1] L. M. Stancanelli, E. Secchi, and M. Holzner, "Magnetic fluid film enables almost complete drag reduction across laminar and turbulent flow regimes," *Communications Physics*, vol. 7, no. 1, Jan. 2024, Art. no. 30, https://doi.org/10.1038/s42005-023-01509-1.

[2] R. V. Abramov, "Turbulence via intermolecular potential: Uncovering the origin," *Communications in Nonlinear Science and Numerical Simulation*, vol. 130, Mar. 2024, Art. no. 107727, https://doi.org/10.1016/j.cnsns.2023.107727.

[3] S. M. Cameron, V. I. Nikora, and I. Marusic, "Drag forces on a bed particle in open-channel flow: effects of pressure spatial fluctuations and very-large-scale motions," *Journal of Fluid Mechanics*, vol. 863, pp. 494–512, Mar. 2019, https://doi.org/10.1017/jfm.2018.1003.

[4] D. Saranadhi, D. Chen, J. A. Kleingartner, S. Srinivasan, R. E. Cohen, and G. H. McKinley, "Sustained drag reduction in a turbulent flow using a low-temperature Leidenfrost surface," *Science Advances*, vol. 2, no. 10, Oct. 2016, Art. no. e1600686, https://doi.org/10.1126/sciadv.1600686.

[5] G. H. Choueiri, J. M. Lopez, and B. Hof, "Exceeding the Asymptotic Limit of Polymer Drag Reduction," *Physical Review Letters*, vol. 120, no. 12, Mar. 2018, Art. no. 124501, https://doi.org/10.1103/PhysRevLett.120.124501.

[6] Y. K. İlter, U. O. Ünal, W. Shi, S. Tokgöz, and M. Atlar, "An experimental investigation into the drag reduction performance of dimpled plates in a fully turbulent channel flow," *Ocean Engineering*, vol. 307, Sep. 2024, Art. no.118198, https://doi.org/10.1016/j.oceaneng.2024.118198.

[7] B. M. A. S. Ali, J. M. S. Suleimany, and S. S. Ibrahim, "Numerical Modeling of the Flow around a Cylinder using FEATool Multiphysics," *Engineering, Technology & Applied Science Research*, vol. 13, no. 4, pp. 11290–11297, Aug. 2023, https://doi.org/10.48084/etasr.6053.

[8] J. R. Welty, C. E. Wicks, R. E. Wilson, and G. Rorrer, *Fundamentals of momentum, heat, and mass transfer*, 5th. ed. Hoboken, NJ: John Wiley & Sons, Incorporated, 2008.

[9] B. J. Rosenberg, T. Van Buren, M. K. Fu, and A. J. Smits, "Turbulent drag reduction over air- and liquid- impregnated surfaces," *Physics of Fluids*, vol. 28, no. 1, Jan. 2016, Art. no. 015103, https://doi.org/10.1063/1.4939272.

[10] S. A. Asghari Pari, S. M. Kashefipour, and M. Ghomeshi, "An experimental study to determine the obstacle height required for the control of subcritical and supercritical gravity currents," *European Journal of Environmental and Civil Engineering*, vol. 21, no. 9, pp. 1080–1092, Sep. 2017, https://doi.org/10.1080/19648189.2016.1144537.

[11] A. D'Ippolito, F. Calomino, A. Fiorini Morosini, and R. Gaudio, "Drag coefficients and water surface profiles in channels with arrays of linear rigid emergent vegetation," *Journal of Hydro-environment Research*, vol. 57, pp. 27–37, Nov. 2024, https://doi.org/10.1016/j.jher.2024.10.001.

[12] B. R. Solomon, K. S. Khalil, and K. K. Varanasi, "Drag Reduction using Lubricant-Impregnated Surfaces in Viscous Laminar Flow," *Langmuir*, vol. 30, no. 36, pp. 10970–10976, Sep. 2014, https://doi.org/10.1021/la5021143.

[13] A. Gijón Mancheño, W. Jansen, J. C. Winterwerp, and W. S. J. Uijttewaal, "Predictive model of bulk drag coefficient for a nature-based structure exposed to currents," *Scientific Reports*, vol. 11, no. 1, Feb. 2021, Art. no. 3517, https://doi.org/10.1038/s41598-021-83035-0.

[14] H. C. Burridge *et al.*, "The transport of liquids in softwood: timber as a model porous medium," *Scientific Reports*, vol. 9, no. 1, Dec. 2019, Art. no. 20282, https://doi.org/10.1038/s41598-019-55811-6.

[15] M. Albers, X. Shao, and W. Schröder, "Energy efficient actuated drag reduced compressible turbulent flat plate flow," *International Journal of Heat and Fluid Flow*, vol. 106, Apr. 2024, Art. no. 109314, https://doi.org/10.1016/j.ijheatfluidflow.2024.109314.

[16] J. Liu, Y. Ju, Y. Zhang, and W. Gong, "Preferential Paths of Air-water Two-phase Flow in Porous Structures with Special Consideration of Channel Thickness Effects," *Scientific Reports*, vol. 9, no. 1, Nov. 2019, Art. no. 16204, https://doi.org/10.1038/s41598-019-52569-9.

[17] M. Kordnaeij, M. Sajadi, and M. S. Bajestan, "Experimentally Comparisons of the Effect of Porous Sheets and Porous Obstacles in Controlling Turbidity Current," *Water and Soil Science*, vol. 27, no. 1, pp. 43–54, May 2017.

[18] I. Widyastuti, M. A. Thaha, R. T. Lopa, and M. P. Hatta, "Dam-Break Energy of Porous Structure for Scour Countermeasure at Bridge Abutment," *Civil Engineering Journal*, vol. 8, no. 12, pp. 3939–3951, Dec. 2022, https://doi.org/10.28991/CEJ-2022-08-12-019.

[19] S. Coleman, "Hydraulics in Civil and Environmental Engineering," *Journal of Hydraulic Engineering*, vol. 126, no. 9, pp. 724–725, Sep. 2000, https://doi.org/10.1061/(ASCE)0733-9429(2000)126:9(724).

[20] J. Abdurrosyid and A. Fatchan, "Gerusan di sekitar abutmen dan pengendaliannya pada kondisi ada angkutan sedimen untuk saluran berbentuk majemuk," *Civil Engineering Dynamics*, vol. 7, pp. 20–29, 2017.

[21] S. Altinakar, W. H. Graf, and E. J. Hopfinger, "Weakly depositing turbidity current on a small slope," *Journal of Hydraulic Research*, vol. 28, no. 1, pp. 55–80, Jan. 1990, https://doi.org/10.1080/00221689009499147.

[22] V. T. Chow, *Open-channel hydraulics*, 1st ed. Caldwell, NJ, USA: Blackburn Press, 1959.

[23] P. S. Atmojo, S. S. Sachro, and H. Budieny, "Penggunaan Analisis Dimensi untuk Mencari Korelasi Antar Variabel pada Uji Model Hidrolik," *Jurnal Teknik Sipil*, vol. 21, no. 3, Dec. 2014, Art. no. 221, https://doi.org/10.5614/jts.2014.21.3.5.

[24] *Pitot Tubes Portable Operating Instruction and Experiment*, Hampshire, UK: Armfield Engineering Teaching & Research Equipment, 2024.